

# Superwind-driven Intense H<sub>2</sub> Emission in NGC 6240 II: Detailed Comparison of Kinematical and Morphological Structures of the Warm and Cold Molecular Gas

Youichi Ohyama,

*Subaru Telescope, National Astronomical Observatory of Japan, 650 N. A'ohoku Place, University Park, Hilo, HI 96720*

Michitoshi Yoshida,

*Okayama Astrophysical Observatory, National Astronomical Observatory of Japan, Kamogata-cho, Asakuchi-gun, Okayama 719-0232, Japan*

and Tadafumi Takata

*Subaru Telescope, National Astronomical Observatory of Japan, 650 N. A'ohoku Place, University Park, Hilo, HI 96720*

## ABSTRACT

We report on our new analysis of the spatial and kinematical distribution of warm and cold molecular gas in the nearby, prototypical, luminous infrared galaxy NGC 6240, which was undertaken to explore the origin of its unusually luminous H<sub>2</sub> emission. The gas components are known to be distributed between the two merging nuclei, forming an off-nuclear molecular gas concentration. By comparing three-dimensional emission-line data (in space and velocity) of CO (J=2 – 1) in the radio and H<sub>2</sub> in the near infrared, we are able to search for the spatial and kinematical conditions under which efficient H<sub>2</sub> emission is produced in much more detail than has previously been possible. In particular, we focus on the H<sub>2</sub> emitting efficiency, defined in terms of the intensity ratio of H<sub>2</sub> to CO [ $I(\text{H}_2)/I(\text{CO})$ ], as a function of velocity. We derive this by utilizing the recent high-resolution three-dimensional data presented by Tecza et al. (2000). The integrated H<sub>2</sub> emitting efficiency is calculated by integrating the velocity profile of H<sub>2</sub> emitting efficiency in blue, red, and total (blue + red) velocity regions of the profile. We find that (1) both the total H<sub>2</sub> emitting efficiency and the blue-to-red ratio of the efficiency are larger in regions surrounding the CO and H<sub>2</sub> intensity peaks, and (2) the H<sub>2</sub> emitting efficiency and the kinematical conditions in the warm molecular gas are closely related to each other. We compare two possible models that might explain these characteristics: a large-scale collision between the molecular gas concentration and the merging nuclei, and a collision between the molecular gas concentration and the external superwind outflow from the southern nucleus. The latter model seems more plausible, since it can reproduce the enhanced emitting efficiency of blueshifted

H<sub>2</sub> around the molecular gas concentration, if we assume that the superwind blows from the southern nucleus toward us, hitting the entire gas concentration from behind. In this model, internal cloud-cloud collisions within the molecular gas concentration are enhanced by the interaction with the superwind outflow, and efficient and intense shock-excited H<sub>2</sub> emission is expected as a result of the cloud-crushing mechanism. The observed spatial distribution of the H<sub>2</sub> emitting efficiency can be explained if there is a greater kinematical disturbance in the outer part of the molecular gas concentration, as a result of the interaction with the superwind outflow, and also more frequent cloud-cloud collisions in the region. In addition, the kinematical influence of the superwind on the molecular gas concentration should be larger at bluer velocities, and the collision frequency is expected to be larger at bluer velocities, explaining the relationship between velocity and the H<sub>2</sub> emitting efficiency.

*Subject headings:* Galaxies: individual (NGC 6240) — Galaxies: interacting — Galaxies: intergalactic medium — Shock waves

## 1. INTRODUCTION

NGC 6240 is a nearby<sup>1</sup> luminous infrared galaxy (e.g., Wright, Joseph & Meikle 1984; Joseph & Wright 1984), comprising two merging nuclei (north and south nuclei: hereafter, N and S nuclei, respectively) separated by 1.9'' (Condon et al. 1982; Fried & Schulz 1983; Eales et al. 1990; Thronson et al. 1990; Herbst et al. 1990; Colbert, Wilson, & Bland-Hawthorn 1994; Sugai et al. 1997; Tacconi et al. 1999; Ohyama et al. 2000; Scoville et al. 2000; Tecza et al. 2000; Beswick et al. 2001), and is well known for its unusually luminous H<sub>2</sub> emission in the near infrared (e.g., Rieke et al. 1985; DePoy, Becklin, & Wynn-Williams 1986). Although many excitation mechanisms for the H<sub>2</sub> have been proposed to date [shock excitation (Rieke et al. 1985; DePoy et al. 1986; Lester, Harvey, & Carr 1988; Elston & Maloney 1990; Herbst et al. 1990; van der Werf et al. 1993; Sugai et al. 1997); UV fluorescence (Tanaka, Hasegawa, & Gatley 1991); X-ray heating (Draine & Woods 1990); and formation pumping (Mouri & Taniguchi 1995)], H<sub>2</sub> line ratio analyses have revealed that shock excitation is responsible for almost all the H<sub>2</sub> emission (Sugai et al. 1997; Ohyama et al. 2000; Tecza et al. 2000). However, because of its huge H<sub>2</sub> luminosity and exceptionally large H<sub>2</sub>/Br  $\gamma$  intensity ratio, the origin of NGC 6240's H<sub>2</sub> emission has been the subject of considerable debate; star formation activity is not strong enough to power all the observed H<sub>2</sub> luminosity (e.g., Rieke et al. 1985; Draine & Woods 1990). Interestingly, most of the H<sub>2</sub> emission comes from the region between the nuclei, although both Br  $\gamma$  and [Fe II] (originating from OB type stars and supernovae in star-forming regions) are detected from each nucleus (Herbst et al. 1990; van der Werf et al. 1993; Sugai et al. 1997; Ohyama et al. 2000; Tecza et al. 2000). Two possible models

---

<sup>1</sup>In this paper, the distance is assumed to be 98 Mpc, following, for consistency, Heckman, Armus, & Miley (1987) and Ohyama et al. (2000).

have been proposed to explain this intense, off-nuclear, shock-excited H<sub>2</sub> emission. In the first, the emission is caused by shock heating at the interface between the two colliding galaxies (Tecza et al. 2000 and references therein), while in the second it is due to the interaction between the hot gas associated with the superwind activity of the S nucleus and the tidally-produced molecular gas concentration between the two nuclei (Ohyama et al. 2000).

Recent high-resolution, sensitive CO observations of NGC 6240 at radio wavelengths have revealed that a significant fraction of the system’s molecular gas is concentrated not at the two nuclei but rather occupies the region between them, forming a massive thick disk with highly turbulent motion (Tacconi et al. 1999). Hereafter we refer to the CO gas between the nuclei as the off-nuclear molecular gas or molecular gas concentration. A violent tidal disturbance during the merging process of the two nuclei could be responsible for the formation of such an off-nuclear molecular gas disk, although the creation of such a massive concentration of gas away from the merging nuclei has no theoretical explanation (e.g., Barnes 2002 and references therein; see also Tecza et al. 2002). The peak of the H<sub>2</sub> emission is located between the S nucleus and the CO peak (Ohyama et al. 2000; Tecza et al. 2000).

The first step in exploring the reason for the source’s unusually intense H<sub>2</sub> emission was the analysis of the velocity field and the excitation conditions of the H<sub>2</sub> lines (Ohyama et al. 2000; Tecza et al. 2000 and references therein). In this paper we take the second step by conducting a detailed comparison of the morphological and kinematical conditions of H<sub>2</sub> and CO lines. This work is motivated by the fact that H<sub>2</sub> and CO are molecular species with different excitation conditions; comparisons of their emission lines should give us some new insights on the conditions under which high H<sub>2</sub> emitting efficiency (H<sub>2</sub> flux per molecular gas content) is likely. Such a comparison has only recently become possible, as a result of the availability of sub-arcsecond, sensitive mapping observations of both CO and H<sub>2</sub>. Tecza et al. (2000) conducted three-dimensional H<sub>2</sub> mapping observations of this galaxy under sub-arcsec seeing conditions, while Tacconi et al. (1999) carried out high-resolution CO ( $J = 2 - 1$ ) mapping observations with a sub-arcsec beam. Both data have been re-sampled to make a direct comparison between the cold and warm molecular gas at the same scale (Tecza et al. 2000). Based on these data, we discuss how H<sub>2</sub> emission can be excited efficiently, focusing on the H<sub>2</sub>/CO intensity ratio as an indicator of the H<sub>2</sub> emitting efficiency.

## 2. Data and Analysis

All data that we analyze in this paper were reproduced from Figure 3 of Tecza et al. (2000), in which grids of both the CO ( $J = 2 - 1$ ) and H<sub>2</sub> velocity profiles were presented. These profiles were reproduced from the original data of both Tecza et al. (2000) and Tacconi et al. (1999) for H<sub>2</sub> and CO, respectively. The velocity resolution of the original H<sub>2</sub> data was 150 km s<sup>-1</sup>, while the spatial resolution was 0.8'' - 1.0'', the seeing conditions at the time of observation (Tecza et al. 2000). In the CO observations, the full width at half maximum (FWHM) of the elliptical Gaussian was beam 0.9'' × 0.5'', while the velocity resolution was 6.5 km s<sup>-1</sup>. These data were re-sampled

onto  $0.6 \times 0.6$  arcsec<sup>2</sup> sub-regions ( $290 \times 290$  pc<sup>2</sup>) around the double nuclei over  $3.6 \times 4.2$  arcsec<sup>2</sup> ( $1.7 \times 2.0$  kpc<sup>2</sup>) regions, and re-sampled at  $140$  km s<sup>-1</sup> velocity resolution (Tecza et al. 2000). These data enabled us to compare the CO and H<sub>2</sub> velocity profiles directly, with a resolution that was sufficient to separate the two merging nuclei and the surrounding regions.

The velocity profiles were integrated over blue and red velocity regions ( $dV \equiv V - V_{\text{sys}} = -300 \sim 0$  km s<sup>-1</sup> and  $dV = 0 \sim 300$  km s<sup>-1</sup> for blue and red, respectively, where  $V_{\text{sys}}$  is the systemic velocity) in each sub-region to measure the blue and red intensities of CO and H<sub>2</sub> [ $I_{\text{blue}}(\text{CO})$ ,  $I_{\text{red}}(\text{CO})$ ,  $I_{\text{blue}}(\text{H}_2)$ , and  $I_{\text{red}}(\text{H}_2)$ ]. The velocity cut-offs at  $dV = \pm 300$  km s<sup>-1</sup> were applied in the integration because it is necessary to measure the intensities in the same velocity range for all sub-regions in order to make a fair comparison of their spatial distribution. We found that some sub-regions had a weak CO intensity at larger velocity offsets from the systemic velocity, so that the intensity could not be accurately measured out to the velocity cut-off. We eliminated the integrated intensity data of the sub-regions from the following analyses if the normalized intensity of CO (normalized to be unity at the CO peak position: see Figure 3 of Tecza et al. (2000) and Figure 2 of this paper) was 0.05 (the typical noise level) or less at the cut-off velocity. The cut-off velocity ( $dV = \pm 300$  km s<sup>-1</sup>) was chosen as a compromise: although a larger cut-off velocity is desirable for studying the properties of the high-velocity gas components, applying a larger ( $dV > 300$  or  $< -300$  km s<sup>-1</sup>) velocity cut-off would discard a larger number of sub-regions due to a lack of useful integrated intensity data. Note that since the observed line widths ( $\sim 1000$  km s<sup>-1</sup> and  $\sim 1600$  km s<sup>-1</sup> for CO and H<sub>2</sub> at full width at zero intensity, respectively: Tacconi et al. 1999; Tecza et al. 2000) are wider than the applied velocity cut-off (at  $dV = \pm 300$  km s<sup>-1</sup>), about 19% and 33% of the total CO and H<sub>2</sub> fluxes fall outside the velocity range for the integration, and were not counted in the analysis that follows. Single Gaussian profile fitting was used to measure the velocities of both lines [ $V(\text{CO})$  and  $V(\text{H}_2)$ ], although some areas show more complicated emission line profiles, such as a double-peaked profile (Tecza et al. 2000). Figure 1 shows the total (blue+red) integrated intensity and the velocity maps of both CO and H<sub>2</sub> [ $I_{\text{blue}}(\text{CO})+I_{\text{red}}(\text{CO})$ ,  $I_{\text{blue}}(\text{H}_2)+I_{\text{red}}(\text{H}_2)$ ,  $V(\text{CO})$ , and  $V(\text{H}_2)$ ]. The peaks of both lines are located between the two nuclei and slightly east of the S nucleus ( $\sim 0.6''$ )<sup>2</sup>. The velocities of both lines change along PA $\sim 45$  deg, in the sense that they are blueshifted around the S nucleus and are redshifted in both the NE and SW regions. Simple models of the velocity field, such as a rotation or a pure expansion/contraction, have difficulty reproducing these observations.

To compare the properties of CO and H<sub>2</sub> emissions, we here introduce a new index, the H<sub>2</sub> emitting efficiency. The efficiency is defined as the intensity ratio of H<sub>2</sub> and CO [ $I(\text{H}_2)/I(\text{CO})$ ], and

---

<sup>2</sup>Note that the higher resolution H<sub>2</sub> map presented by Tecza et al. (2000) and other previous H<sub>2</sub> maps (e.g., Sugai et al. 1997) showed the H<sub>2</sub> peak between the double nuclei, although our Figure 1 shows the peak at a slightly different position. This is an artefact that was probably caused by the re-sampling of the data onto the  $0.6'' \times 0.6''$  sub-regions adopted in producing Figure 3 of Tecza et al. (2000) and our Figure 1. A similar artefact is also seen in the map of CO. The adopted velocity range for integrating the profiles (from  $dV = -300$  km s<sup>-1</sup> to  $dV = 300$  km s<sup>-1</sup>) may also affect the positions of the CO and H<sub>2</sub> peaks in our maps.

was calculated over the entire velocity range on each sub-region (Figure 2). Note, however, that these ratios are shown only at velocities where the normalized CO intensity is larger than 0.05 (the typical noise level) to avoid obtaining erroneous ratios in regions or velocities where CO is weak. Next, the integrated H<sub>2</sub> emitting efficiencies for blue [ $R_{\text{blue}} \equiv \int I(\text{H}_2)/I(\text{CO})dV/\Delta V$ , integrating over the range  $dV = -300$  to  $0 \text{ km s}^{-1}$ ], for red ( $R_{\text{red}}$ , integrating over the range  $dV = 0$  to  $+300 \text{ km s}^{-1}$ ), and for blue plus red (total) ( $R_{\text{total}}$ , integrating over the range  $dV = -300$  to  $+300 \text{ km s}^{-1}$ ) were calculated, in order to examine the spatial and velocity distributions of the efficiencies. Here  $\Delta V$  is the velocity range for the integration, i.e.,  $\Delta V = 300 \text{ km s}^{-1}$  for blue- and red-, and  $\Delta V = 600 \text{ km s}^{-1}$  for total-integrated H<sub>2</sub> emitting efficiencies. A velocity cut-off (at  $dV = \pm 300 \text{ km s}^{-1}$ ) was applied in integrating the H<sub>2</sub> emitting efficiency, in the same way as for the calculation of the integrated intensities. Also, the integrated H<sub>2</sub> emitting efficiencies in sub-regions where the normalized intensity of CO at the cut-off velocity was less than 0.05 were not used in the following analysis. The blue-to-red ratio of the H<sub>2</sub> emitting efficiency ( $R_{\text{blue}}/R_{\text{red}}$ ) could then be calculated. These values ( $R_{\text{total}}$  and  $R_{\text{blue}}/R_{\text{red}}$ ) are mapped together with the velocity difference between CO and H<sub>2</sub> [ $\Delta V_{\text{H}_2-\text{CO}} \equiv V(\text{H}_2) - V(\text{CO})$ ] in Figure 3.

Figure 3 illustrates our main results: (1) The total H<sub>2</sub> emitting efficiency ( $R_{\text{total}}$ ) is smaller around the CO peak, and becomes higher with distance from the peak; (2) the blue-to-red ratio of the H<sub>2</sub> emitting efficiency ( $R_{\text{blue}}/R_{\text{red}}$ ) is smaller around the CO peak, and becomes larger with distance from the peak; and (3) the velocity difference ( $\Delta V_{\text{H}_2-\text{CO}}$ ) is smaller around the CO peak, while the H<sub>2</sub> emission becomes more blueshifted with respect to CO with distance from the peak. All these trends are seen almost systematically as a function of position, and are evident well over our resolution ( $\sim 0.6''$  in space and  $140 \text{ km s}^{-1}$  in velocity). It seems noteworthy that the peak of H<sub>2</sub> emitting efficiency corresponds neither to the peak position of CO nor to that of H<sub>2</sub>.

We searched for correlations between the measured quantities ( $R_{\text{total}}$  and  $R_{\text{blue}}/R_{\text{red}}$ ); the results are shown in Figures 4 and 5. In these plots, data are marked with different symbols for different groups of sub-regions, which were divided according to their spatial positions around the CO intensity peak: the central region with higher H<sub>2</sub> and CO intensities between the two nuclei (nuclear region), the region northeast of the central region (NE region), and the southwestern region (SW region). Two other sub-regions, the most southwesterly regions where H<sub>2</sub> intensity increases with distance from the nucleus (the SW sub-group) and the most northeasterly regions with double-peaked profiles (the NE sub-group), are grouped separately. These sub-regions are also indicated in Figure 2. We found a tight negative correlation between  $I(\text{CO})$  and  $R_{\text{total}}$  (Figure 4). A Spearman rank-order test for the correlation between  $\log[R_{\text{total}}]$  and  $\log[I(\text{CO})]$  showed that the probability  $P$  of consistency with the null hypothesis (i.e., no correlation between the two quantities) is less than 0.001 for any sub-grouping (all the regions, all the regions except the SW sub-group, and all regions except for both SW and NE sub-groups). Therefore we consider that we have definitely shown that the total H<sub>2</sub> emitting efficiency is enhanced in the outer regions with weaker CO emission. Two other positive correlations were found, between  $\Delta V_{\text{H}_2-\text{CO}}$ ,  $R_{\text{blue}}/R_{\text{red}}$ , and  $R_{\text{total}}$  (Figure 5). Although these correlations look less tight, a Spearman rank order test

showed that the probability  $P$  of the null hypothesis is 0.20, 0.02, and 0.04 for the above three sub-groupings, respectively, in  $\Delta V_{\text{H}_2\text{-CO}}$  vs.  $R_{\text{blue}}/R_{\text{red}}$  diagram, and 0.02, 0.001, and  $<0.001$  for the same three sub-groupings, respectively, in  $\Delta V_{\text{H}_2\text{-CO}}$  vs.  $R_{\text{total}}$  diagram, indicating the presence of significant correlations between these quantities at greater than the 98% significance level if we exclude the SW sub-group.

### 3. DISCUSSION

#### 3.1. H<sub>2</sub> Excitation Mechanism

Our analysis has shown that the H<sub>2</sub> emitting efficiency and the kinematical conditions of the warm gas are closely related. Such a correlation is a good indication of shock heating, in which bulk kinetic energy is converted to energy radiated through the H<sub>2</sub> line. Although our analyses were carried out only for fluxes within the velocity range of  $dV = -300 \sim 300 \text{ km s}^{-1}$ , it seems reasonable to interpret the correlation as an indication of the major mechanism of the excitation of H<sub>2</sub>, because this velocity range contains 81% and 67% of the total fluxes of CO and H<sub>2</sub>, respectively (see Section 2 above). In some inner sub-regions where we can trace the H<sub>2</sub> emitting efficiency at even bluer velocities ( $dV < -300 \text{ km s}^{-1}$ ), we found that the efficiency is generally higher at bluer velocity ( $dV < -300 \text{ km s}^{-1}$ ) than at lower velocity ( $dV = -300 \sim 0 \text{ km s}^{-1}$ ), and this fact supports a model in which shock excitation of H<sub>2</sub> is a major excitation mechanism around NGC 6240. Although other H<sub>2</sub> excitation mechanisms (e.g., UV fluorescence, X-ray heating, and formation pumping) cannot be rejected, their contribution to the total must be less important. We note that the same conclusion has previously been reached based on a line-ratio analysis of the near-infrared spectra (Sugai et al. 1997; Tecza et al. 2000; and Ohyama et al. 2000).

#### 3.2. The Superwind Model

Since correlations between the H<sub>2</sub> emitting efficiency and the kinematical conditions of the molecular gas were found not only on the SW but also on the NE side of the CO peak, on scales of  $2''$ , the molecular gas concentration seems likely to be surrounded by gas that has a simple global motion. The motion is probably directed predominantly toward the observer, and the interaction between the gas that has this blueshifted motion and the molecular gas concentration would increase the H<sub>2</sub> emitting efficiency on the bluer velocity side of the CO emission. The question then arises: what is the origin of this blueshifted gas motion? In the following, we discuss two possible explanations.

One possibility is that the merging nuclei are interacting with the off-nuclear molecular gas as they rotate around each other. Although there are no good theoretical explanations for the formation of such an off-nuclear molecular gas concentration in merging galaxies (e.g., Barnes 2002

and references therein; see also Tecza et al. 2002), here we assume that such concentration has formed as a result of tidal effects during the merging process. Since the  $\text{H}_2$  emitting efficiency is relatively higher at the SW portion of the concentration, a collision between the S galaxy and the concentration might contribute to the excitation of  $\text{H}_2$  emission. The extinction maps (Scoville et al. 2000; Tecza et al. 2000) have revealed the presence of a dusty region at  $0'' - 1.0''$  NNE of the S nucleus, and the position of the maximum extinction ( $\sim 0.2'' - 0.3''$  NNE of the S nucleus) coincides spatially with the CO peak. This indicates that the S galaxy is behind the dusty molecular gas concentration from our point of view. Since the S nucleus is known to be moving toward us around the concentration (Fried & Ulrich 1985; Tecza et al. 2000), a violent collision between the two would enhance the blueshifted  $\text{H}_2$  emission at the SW side of the CO peak. If this is the case, however, the redshifted  $\text{H}_2$  emission, rather than the blueshifted component, would be enhanced on the opposite side of the CO peak, because the N galaxy is rotating away from us on the opposite side of the concentration. This model therefore cannot explain the fact that blue-enhanced  $\text{H}_2$  emitting efficiency is observed on both sides of the CO peak.

The alternative model is that an outflow associated with the superwind activity of the S nucleus interacts with the off-nuclear molecular gas concentration. The superwind activity of this galaxy has been recognized as a result of its large-scale ( $\sim 20$  kpc) shock-excited filamentary nebulae (e.g., Armus, Heckman, & Miley 1990; Keel et al. 1990) and the expanding motion of the  $\text{H}_2$  emitting clouds around the nuclear region (Ohyama et al. 2000). Since both of the individual galaxies are known to show flat rotation curves in their stellar velocity fields (Tecza et al. 2000), disk structures are likely to be present around each nucleus, even though the system is an advanced merger. Therefore we expect any superwind outflow to exhibit a bi-directional conical shape pointing toward the disk polar direction (e.g., Tomisaka & Ikeuchi 1988; Heckman et al. 1990; Suchkov et al. 1994; Strickland & Stevens 2000), although the shape of the outflow might be distorted due to the inhomogeneous distribution of the medium around the nucleus. An  $H$ -band image of the S nucleus reveals an elongated structure in the NW-SE direction, suggesting the presence of a disk whose minor axis is directed NE-SW at an inclination angle of  $i \simeq 60$  deg (Scoville et al. 2000; Tecza et al. 2000). Also, as mentioned earlier, the S nucleus seems to be located behind the molecular gas concentration. Assuming that the off-nuclear molecular gas concentration formed during the merging process of the two nuclei, before the superwind started to blow, we would expect that, if a bi-conical superwind outflow emanated from the S nucleus, it would interact with the gas concentration from the rear. This interaction would produce blueshifted  $\text{H}_2$  emission around the CO peak (i.e., not only at the SW but also at the NE sides of the CO peak) if the opening angle of the outflow were wide enough to cover the whole molecular gas concentration. The oppositely directed cone of the superwind, pointing away from us, would not contribute significantly to the  $\text{H}_2$  luminosity, as it would not interact with the off-nuclear molecular gas. Since this model has no major difficulties in reproducing the observations, we regard it as more plausible than the model in which the S nucleus is colliding with the molecular gas concentration. A schematic picture of the superwind model is shown in Figure 6. Note that the real situation would be much more complicated due to the complicated medium distribution around the merging nuclei.

Following Heckman et al. (1993), clouds accelerated by the superwind outflow will have a terminal velocity of  $v_{\text{cloud}} = 400 L_{\text{bol}, 11}^{1/2} r_{\text{kpc}}^{-1/2} N_{21}^{-1/2} \text{ km s}^{-1}$ , where  $L_{\text{bol}, 11}$  is the bolometric luminosity in units of  $10^{11} L_{\odot}$ ,  $r_{\text{kpc}}$  is the initial distance of the cloud from the nucleus, and  $N_{21}$  is the column density of the interstellar clouds in units of  $10^{21} \text{ cm}^{-2}$ . Adopting  $L_{\text{bol}, 11} = 4.6$  (Sanders & Mirabel 1995),  $r \sim 1.0 \text{ kpc}$  (the projected distance between the S nucleus and the CO peak multiplied by a de-projection factor of  $\sim 2$ ), and  $N_{21} = 1 - 20^3$ , this equation implies that the clouds would be blown off at a speed of between a few and several hundreds of  $\text{km s}^{-1}$ , which is almost comparable to the observed line width of  $\text{H}_2$  ( $\sim 500 \text{ km s}^{-1}$  in FWHM: e.g., Ohyama et al. 2000; Tecza et al. 2000) and CO ( $\sim 260 - 400 \text{ km s}^{-1}$  in FWHM: Tacconi et al. 1999). Since the column density is likely to decline outward around the CO peak, falling off in a similar way to the CO surface brightness, (Figure 1a)<sup>4</sup>, i.e., the column density of each cloud is larger near the CO peak and is smaller at the outer region, so that clouds in the outer part of the molecular gas concentration would be accelerated up to faster speeds than those near to the CO peak. Therefore the observed trend in the relatively blueshifted  $\text{H}_2$  emission with respect to the CO emission in the outer part of the molecular gas concentration can be explained naturally by the model of superwind-molecular gas concentration interaction. This fact further suggests that kinematical disturbance due to the superwind also raises the  $\text{H}_2$  emitting efficiency within the molecular gas concentration, given the positive correlation between the  $\text{H}_2$  emitting efficiency and  $\Delta V_{\text{H}_2-\text{CO}}$ .

It has been pointed out that a C-type shock ( $v_{\text{shock}} \lesssim 40 \text{ km s}^{-1}$ ), rather than a J-type shock with faster shock velocity, is responsible for exciting most of the  $\text{H}_2$  emission, although most of the emission comes from clouds within a faster global velocity field ( $dV > 100 \text{ km s}^{-1}$ ) (Sugai et al. 1997). One way to resolve this apparent contradiction is to suggest that internal cloud-cloud collisions within the clumpy medium, at speeds of  $\sim 30-50 \text{ km s}^{-1}$ , excite the  $\text{H}_2$  emission, while the clouds move along the global velocity field as a whole (Tecza et al. 2000). Since the molecular gas concentration is known to form a turbulent thick rotating disk (Tacconi et al. 1999), it is likely that the concentration is actually composed of numerous smaller clouds (Tecza et al. 2000). A high-resolution velocity dispersion map of the CO (Figure 4 of Tacconi et al. 1999) reveals the presence of regions with higher velocity dispersion just around the CO peak (especially to the SE and NW sides of the CO peak). Therefore it seems very likely that the interaction of small clouds within the molecular gas concentration with the external superwind provides an enhanced random velocity at the outer part of the CO concentration, as well as the blueshift of the  $\text{H}_2$  with respect to the CO.

---

<sup>3</sup>Here we adopt  $N_{21} = 1$  as a minimum acceptable value corresponding to the typical value for the Milky Way. We also adopt  $N_{21} \sim 20$  as a maximum acceptable value corresponding to one tenth of the total column density inferred from molecular gas observations of  $N_{21} \gtrsim 200$  (Tacconi et al. 1999).

<sup>4</sup>The total column density of the molecular gas integrated over the line of sight is proportional to the observed integrated CO intensity, so the total CO intensity map is similar to the map of the total column density. Although the column density of each cloud may not be proportional to the total one, they are likely to be almost proportional to each other if we assume a simple homogeneous distribution of small clouds within the molecular gas concentration.



### 3.3. The Cloud-Crushing Model

One of the merits of utilizing cloud-cloud collisions within the molecular gas concentration to give rise to the H<sub>2</sub> emission is that a higher efficiency of energy deposition into the molecular gas clouds from the supernova explosions can be expected as a result of the cloud-crushing mechanism (Cowie, McKee, & Ostriker 1981), and the observed huge H<sub>2</sub> luminosity can be explained (Draine & Woods 1990; Elston & Maloney 1990). This therefore raises the question of whether the observed trends in H<sub>2</sub> emitting efficiency, as well as the total H<sub>2</sub> luminosity, can be explained in terms of the cloud-crushing mechanism. In this model, we may consider, as a simple case, that some fraction of the kinetic energy of the small clouds, randomly moving within the bulk motion of the rotating molecular gas concentration, is dissipated through internal shocks as a result of cloud-cloud collisions, and gives rise to H<sub>2</sub> emission. Then, the H<sub>2</sub> surface brightness at a velocity of  $v$  can be expressed as  $I_{\text{H}_2}(v) = 0.5\Sigma_{\text{H}_2}(v)\zeta(v) \langle v_{\text{internal}}^2 \rangle \epsilon/\Delta t$ , where  $\Sigma_{\text{H}_2}(v)$  is the surface mass density of the molecular gas concentration whose velocity is  $v$ ,  $\zeta(v)$  is the mass fraction of the small clouds that give rise to H<sub>2</sub> emission through the cloud-crushing mechanism at a velocity  $v$ ,  $\langle v_{\text{internal}}^2 \rangle$  is the mean of the squared internal random velocity of the small clouds,  $\epsilon$  is the fraction of the energy dissipated in the shock which is radiated in the H<sub>2</sub> 1-0  $S(1)$  line, and  $\Delta t$  is the timescale of the cloud-cloud collisions. Since the surface mass density of the clouds  $\Sigma_{\text{H}_2}(v)$  is proportional to the observed CO surface brightness  $[I_{\text{CO}}(v)]$  at the velocity of  $v$ , the H<sub>2</sub> emitting efficiency can be expressed as  $I_{\text{H}_2}(v)/I_{\text{CO}}(v) \propto \zeta(v) \langle v_{\text{internal}}^2 \rangle \epsilon/\Delta t$ , by definition. Since we are considering a situation in which the cloud-crushing mechanism is responsible for *all* the H<sub>2</sub> emission, we may substitute a constant  $\epsilon$  ( $\simeq 0.3$ ) and a constant internal velocity ( $\langle v_{\text{internal}}^2 \rangle^{1/2} = 40 - 50 \text{ km s}^{-1}$ ) into the equation, representing an extreme case of the cloud-crushing mechanism working at its maximum efficiency (Draine & Woods 1990). Then, the H<sub>2</sub> emitting efficiency can be expressed as  $I_{\text{H}_2}(v)/I_{\text{CO}}(v) \propto \zeta(v)/\Delta t$ . This expression indicates that the H<sub>2</sub> emitting efficiency is higher when (1) a larger mass fraction of the clouds is involved in the production of H<sub>2</sub> emission through the cloud-crushing mechanism, and/or (2) the collision frequency is higher (i.e., the collision timescale is shorter). The observed close relationship between the H<sub>2</sub> emitting efficiency and the kinematical conditions in the molecular gas clouds can be explained by this expression, if the cloud-crushing mechanism is efficient: The outer part of the off-nuclear molecular-gas concentration is likely to be more strongly influenced kinematically by the interaction with the external superwind (see Section 3.2 above), and the H<sub>2</sub> emitting efficiency is expected to be higher, since a larger mass fraction of the clouds will produce H<sub>2</sub> as a result of internal cloud-cloud shocks and a higher frequency of the cloud-cloud collisions. In addition, the efficiency is expected to be higher at bluer velocities, because these are likely to be caused as a result of a more violent kinematical influence from the superwind. Therefore, the cloud-crushing mechanism within a molecular gas concentration disturbed by the interaction with the external superwind outflow seems to be able to reproduce the observed trends of the H<sub>2</sub> emitting efficiency in both space and velocity, as well as the higher-than-normal H<sub>2</sub> luminosity. Although the mechanism by which the off-nuclear molecular gas concentration between the two merging nuclei is created is not clear, the presence of such a gas concentration is necessary if the model is to reproduce the observed intense and efficient H<sub>2</sub> emission. We look forward to

future theoretical studies of the origin of such a gas concentration.

We thank Matthias Tecza who kindly allowed us to see his doctoral thesis and gave us useful comments on the “Data and Analysis” section of this paper.

## REFERENCES

- Armus, L., Heckman, T. M., & Miley, G. K. 1990, ApJ, 364, 471
- Barnes, J. E. 2002, MNRAS, 333, 481
- Beswick, R. J., Pedlar, A., Mundell, C. G., & Gallimore, J. F. 2001, MNRAS, 325, 151
- Colbert, E. J. M., Wilson, A. S., & Bland-Hawthorn, J. 1994, ApJ, 436, 89
- Condon, J. J., Condon, M. A., Gisler, G., & Puschell, J. J. 1982, ApJ, 252, 102
- Cowie, L. L., McKee, C. F., & Ostriker, J. P. 1981, ApJ, 247, 908
- DePoy, D. K., Becklin, E. E., Wynn-Williams, C. G. 1986, ApJ, 307, 116
- Draine, B. T., & Woods, D. T. 1990, ApJ, 363, 464
- Eales, S. A., Becklin, E. E., Hodapp, K.-W., Simons, D. A., & Wynn-Williams, C. G. 1990, ApJ, 365, 478
- Elston, R., & Maloney, P. 1990, ApJ, 357, 91
- Fried, J. W., & Schulz H. 1983, A&A, 118, 166
- Fried, J. W., & Ulrich H. 1985, A&A, 152, L14
- Heckman, T. M., Armus, L., & Miley, G. K. 1987, AJ, 92, 276
- Heckman, T. M., Armus, L., & Miley, G. K. 1990, ApJS, 833, 74
- Heckman, T. M., Lehnert, M. D., & Armus, L. 1993, in *The Environment and Evolution of Galaxies*, eds. J. M. Shull & Thronson, H. A., 455
- Herbst, T. M., Graham, J. R., Beckwith, S., Tsutsui, K., Soifer, B. T., & Matthews, K. 1990, AJ, 99, 1773
- Joseph, R. D., & Wright, G. S. 1985, MNRAS, 214, 87
- Keel, W. C. 1990, AJ, 100, 356
- Lester, D. F., Harvey, P. M., & Carr, J. 1988, ApJ, 329, 641
- Mouri, H., & Taniguchi, Y. 1995, ApJ, 449, 134
- Ohyama, Y., Yoshida, M., Takata, T., Imanishi, M., Usuda, T., et al. 2000, PASJ, 52, 563
- Rieke, G. H., Cutri, R. M., Black, J. H., Kailey, W. F., McAlary, C. W., Lebofsky, M. J., & Elston, R., 1985, ApJ, 290, 116

- Sanders, D. B., & Mirabel, I. F. 1985, *ApJ*, 298, 31
- Scoville, N. Z., Evans, A. S., Thompson, R., Rieke, M., Hines, D. C., Low, F. J., Dinshaw, N., Surace, J. A., & Armus, L. 2000, *AJ*, 119, 991
- Strickland, D. K., & Stevens, I. R. 2000, *MNRAS*, 314, 511
- Suchkov, A. A., Balsara, D. S., Heckman, T. M., & Leitherer, C. 1994, *ApJ*, 430, 511
- Sugai, H., Malkan, M. A., Ward, M. J., Davies, R. I., & McLean I. S. 1997, *ApJ*, 481, 186
- Tacconi, L. J., Genzel, R., Tecza, M., Gallimore, J. F., Downes, D., & Scoville, N. Z. 1999, *ApJ*, 524, 732
- Tanaka, M., Hasegawa, T., & Gatley, I. 1991, *ApJ*, 374, 516
- Tecza, M., Genzel, R., Tacconi, L. J., Anders, S., Tacconi-Garman, L. E., & Thatte, N. 2000, *ApJ*, 537, 178
- Thronson, H. A. Jr., Majewski, S., Descartes, L., & Hereld, M. 1990, *ApJ*, 364, 456
- Tomisaka, K., & Ikeuchi, S. 1988, *ApJ*, 330, 695
- van der Werf, P. P., Genzel, R., Krabbe, A., Blietz, M., Lutz, D., Drapatz, S., Ward, M. J., & Forbes, D. A. 1993, *ApJ*, 405, 522
- Wright, G. S., Joseph, R. D., & Meikle, W. P. S. 1984, *Nature*, 309, 430

Fig. 1.— Maps of the total integrated intensities and velocities of CO and H<sub>2</sub>. North is up, and east is to the left. The positions of the N and S nuclei and the peak position of CO are marked in all plots. Regions where valid data are not available are left blank in these maps. See the main text for the data selection criteria. (a) A map of total integrated CO intensity distribution. The map is shown in a linear scale with contours at an interval of an arbitrary constant. (b) Same as (a), but for H<sub>2</sub>. The map is shown in a linear scale with contours at an interval of an arbitrary constant. (c) A map of CO velocity. Red and blue colors indicate redshifted and blueshifted velocities. The map is shown in a linear scale with contours at constant intervals of 40 km s<sup>-1</sup>. Small numbers within the map indicate the velocity with respect to the systemic velocity in units of km s<sup>-1</sup>. (d) Same as (c), but for H<sub>2</sub>. The contours are drawn at constant intervals of 40 km s<sup>-1</sup>.

Fig. 2.— Velocity profiles of CO (black), H<sub>2</sub> (blue), and H<sub>2</sub>/CO intensity ratio (red) at various positions. Each plot shows the profiles integrated over 0.6'' by 0.6'' sub-regions, taken from Figure 3 of Tecza et al. (2000). The intensity profiles of both CO and H<sub>2</sub> are normalized at the position of the CO peak. The scale for both CO and H<sub>2</sub> profiles is shown on the left side, and that for H<sub>2</sub>/CO intensity ratio profile is shown on the right side. The regions are grouped into five sub-regions, and are shown with different symbols: the central region with higher H<sub>2</sub> and CO intensities around the two nuclei (double circles), the northeastern region from the central region (filled squares), the southwestern region (open squares), the most southwesterly region, where

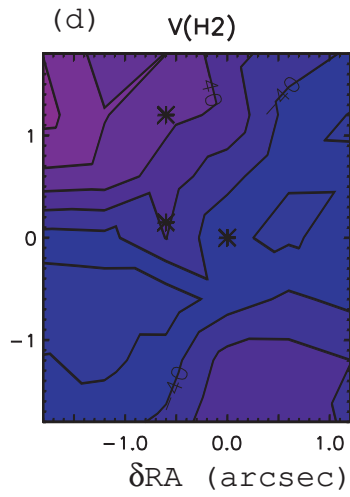
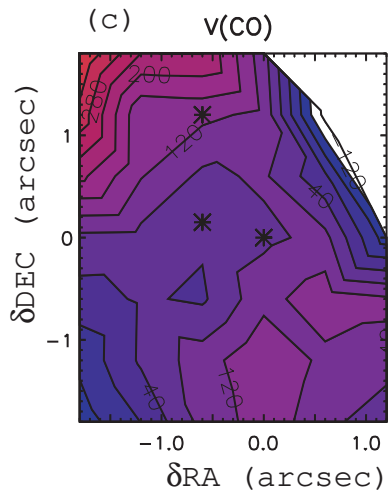
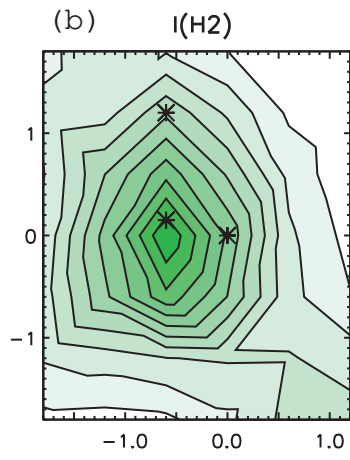
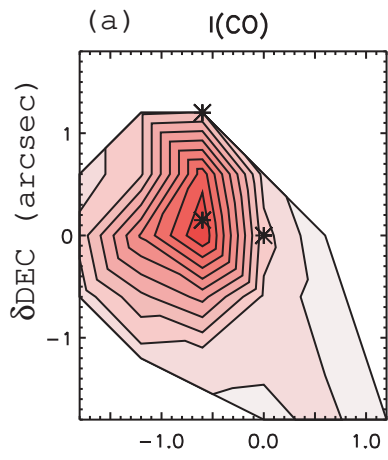
H<sub>2</sub> intensity increases with distance from the nuclei (upper triangle), and the most northeasterly region, with double-peaked profiles (lower triangle). Regions without any marks are not used in the correlation analyses in Figures 4 and 5, where a CO velocity profile is not available out to the velocity cut-off at  $\pm 300$  km s<sup>-1</sup>. See the main text for a discussion of the velocity cut-off.

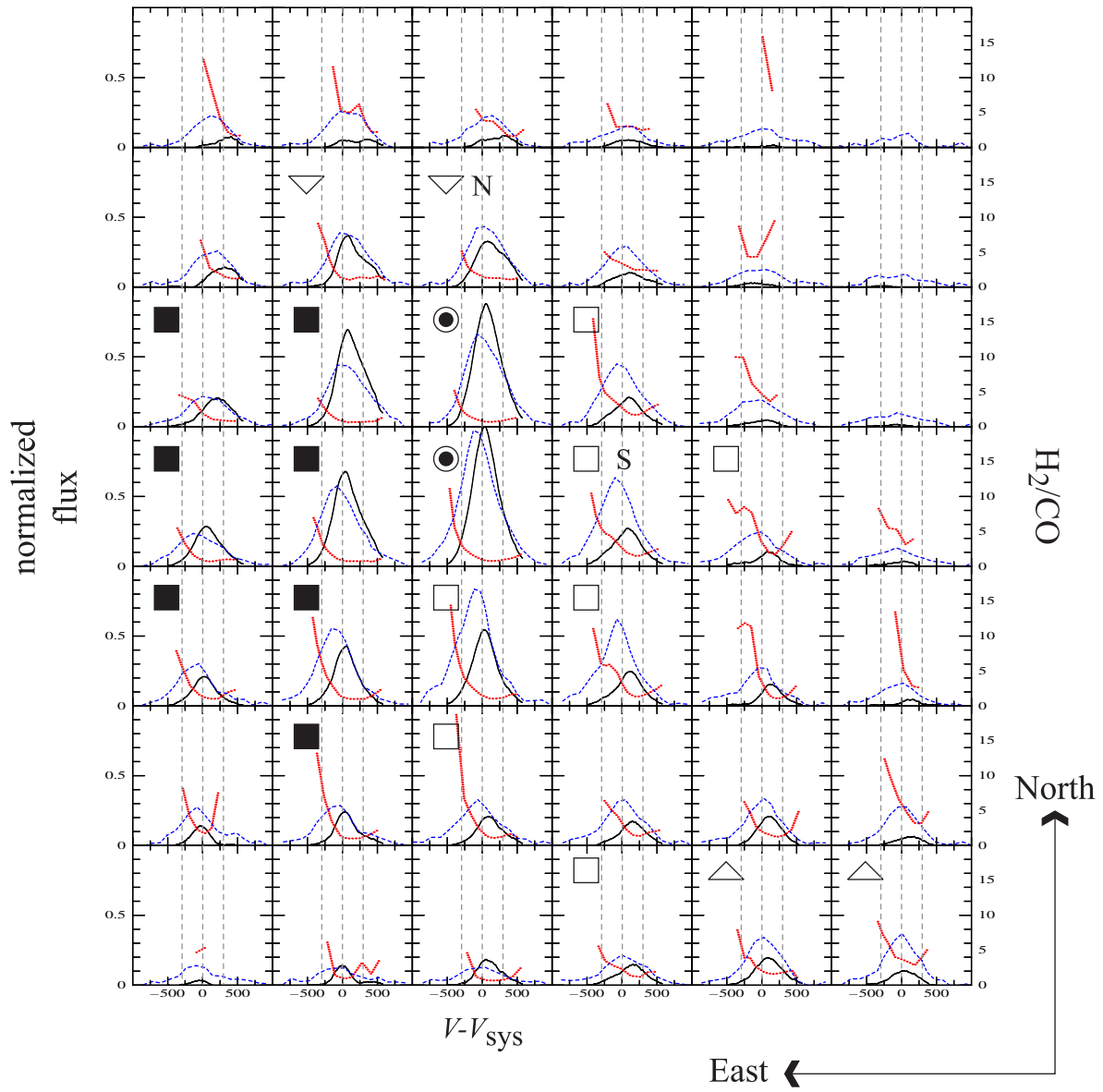
Fig. 3.— Maps of the H<sub>2</sub> emitting efficiencies and the velocity difference between H<sub>2</sub> and CO. North is up, and east is to the left. The positions of the N and S nuclei and the CO peak are marked in all plots. (a) Total integrated CO intensity distribution. This map is the same as Figure 1 (a), but is shown here again for ease of comparison with other maps. (b) A map of the velocity difference between CO and H<sub>2</sub> ( $\Delta V_{\text{H}_2-\text{CO}}$ ). The blue color indicates the region where H<sub>2</sub> is relatively blueshifted with respect to CO. Small numbers within the map indicate  $\Delta V_{\text{H}_2-\text{CO}}$  in units of km s<sup>-1</sup>. Contours are drawn at constant intervals of 20 km s<sup>-1</sup>. (c) A map of the total H<sub>2</sub> emitting efficiency ( $R_{\text{total}}$ ). The green color indicates regions with larger  $R_{\text{total}}$ . Small numbers within the map indicate  $R_{\text{total}}$ . The minimum contour drawn near the S nucleus is drawn at  $R_{\text{total}} = 1.25$ , and other contours are drawn at constant intervals of  $\delta R_{\text{total}} = 0.5$ . (d) A map of the blue-to-red ratio of the H<sub>2</sub> emitting efficiency ( $R_{\text{blue}}/R_{\text{red}}$ ). The blue color indicates the region with relatively enhanced  $R_{\text{blue}}$  over  $R_{\text{red}}$ . Small numbers within the map indicate  $R_{\text{blue}}/R_{\text{red}}$ . The minimum contour drawn between the two nuclei is drawn at  $R_{\text{blue}}/R_{\text{red}} = 2.0$ , and other contours are drawn at constant intervals of  $\delta R_{\text{blue}}/R_{\text{red}} = 0.2$ .

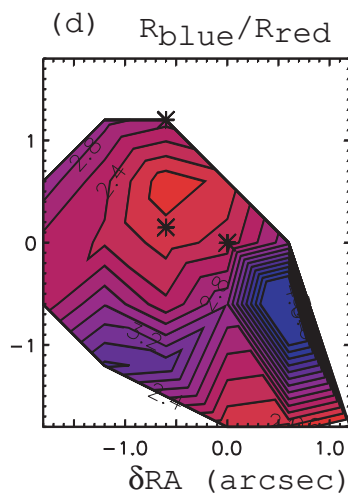
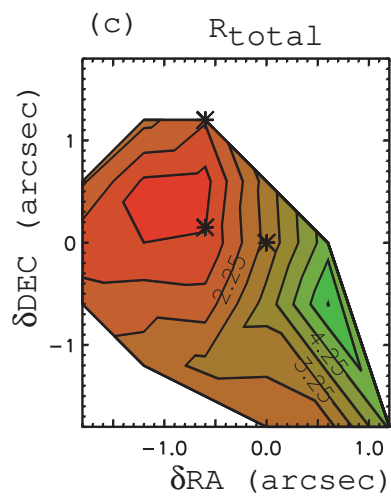
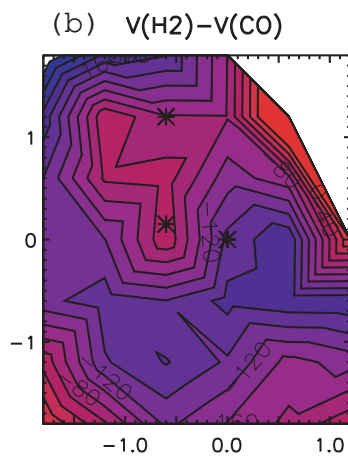
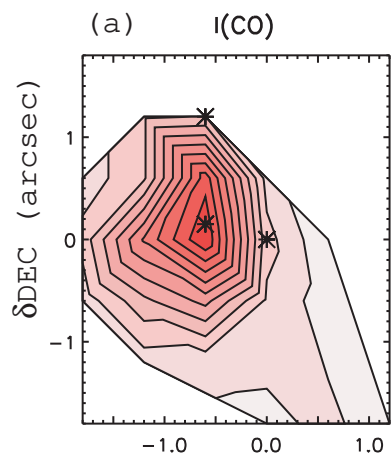
Fig. 4.— The correlation between integrated CO intensity [ $I(\text{CO})$ ] and total H<sub>2</sub> emitting efficiency ( $R_{\text{total}}$ ). The units of  $I(\text{CO})$  are arbitrary. Both axes are shown on a logarithmic scale. Data are plotted with different symbols according to the sub-region from which they come, as shown in Figure 2.

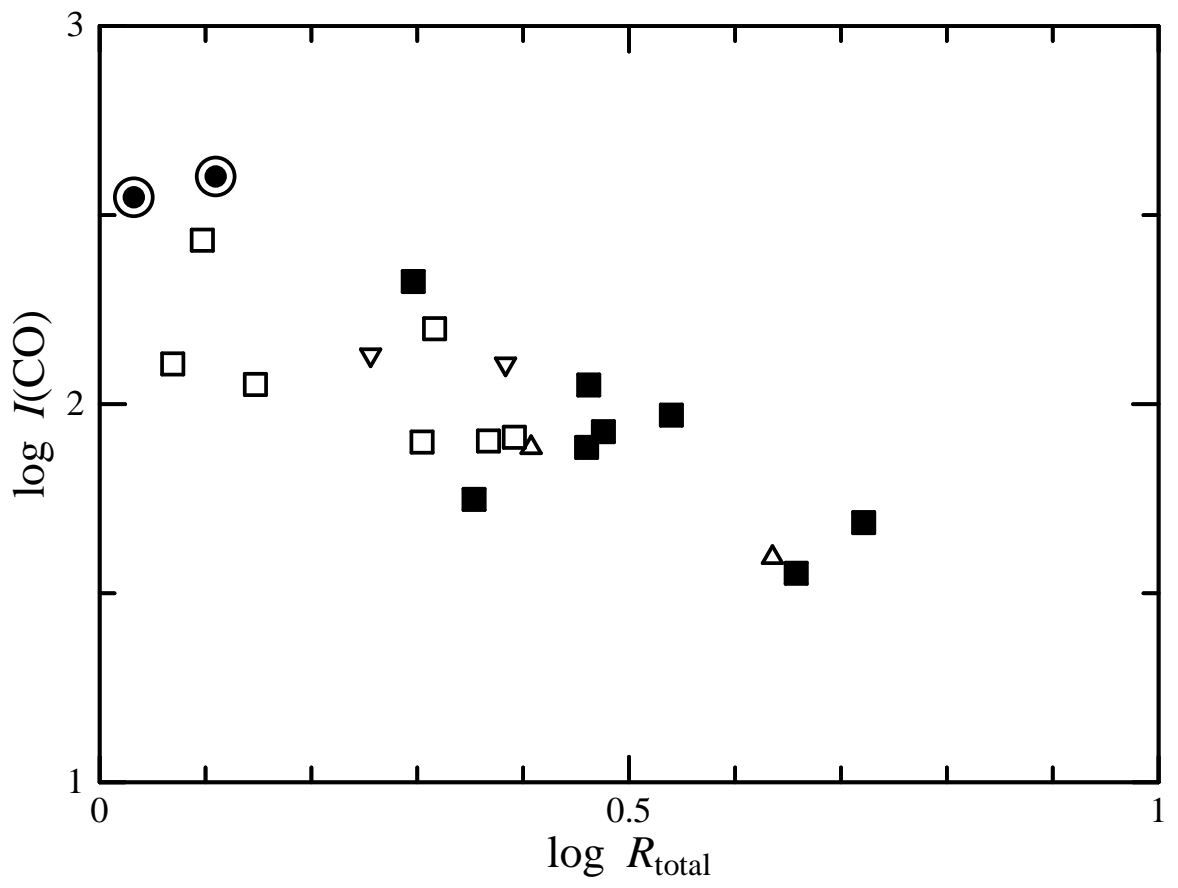
Fig. 5.— Plots of the blue-to-red ratio of the H<sub>2</sub> emitting efficiency ( $R_{\text{blue}}/R_{\text{red}}$ ) and the velocity difference between CO and H<sub>2</sub> ( $\Delta V_{\text{H}_2-\text{CO}}$ ) as a function of the total H<sub>2</sub> emitting efficiency ( $R_{\text{total}}$ ). The symbols used are the same as in Figures 2 and 4.

Fig. 6.— A proposed schematic picture of the superwind model of NGC 6240 seen from our point of view (left) and from the side (right). The two galactic nuclei are rotating around the off-nuclear molecular gas concentration. One of the bi-directional cones of the superwind from the S nucleus (blue) points towards us and interacts with the off-nuclear molecular gas concentration. The interaction between the superwind and the concentration causes the cloud-crushing mechanism to work efficiently in the region between the S nucleus and the concentration (green). Another cone flowing in the opposite direction from the S nucleus (red) would not give rise to such efficient H<sub>2</sub> emission, as there is no off-nuclear molecular gas on this side. See the main text for a more detailed discussion of the model.

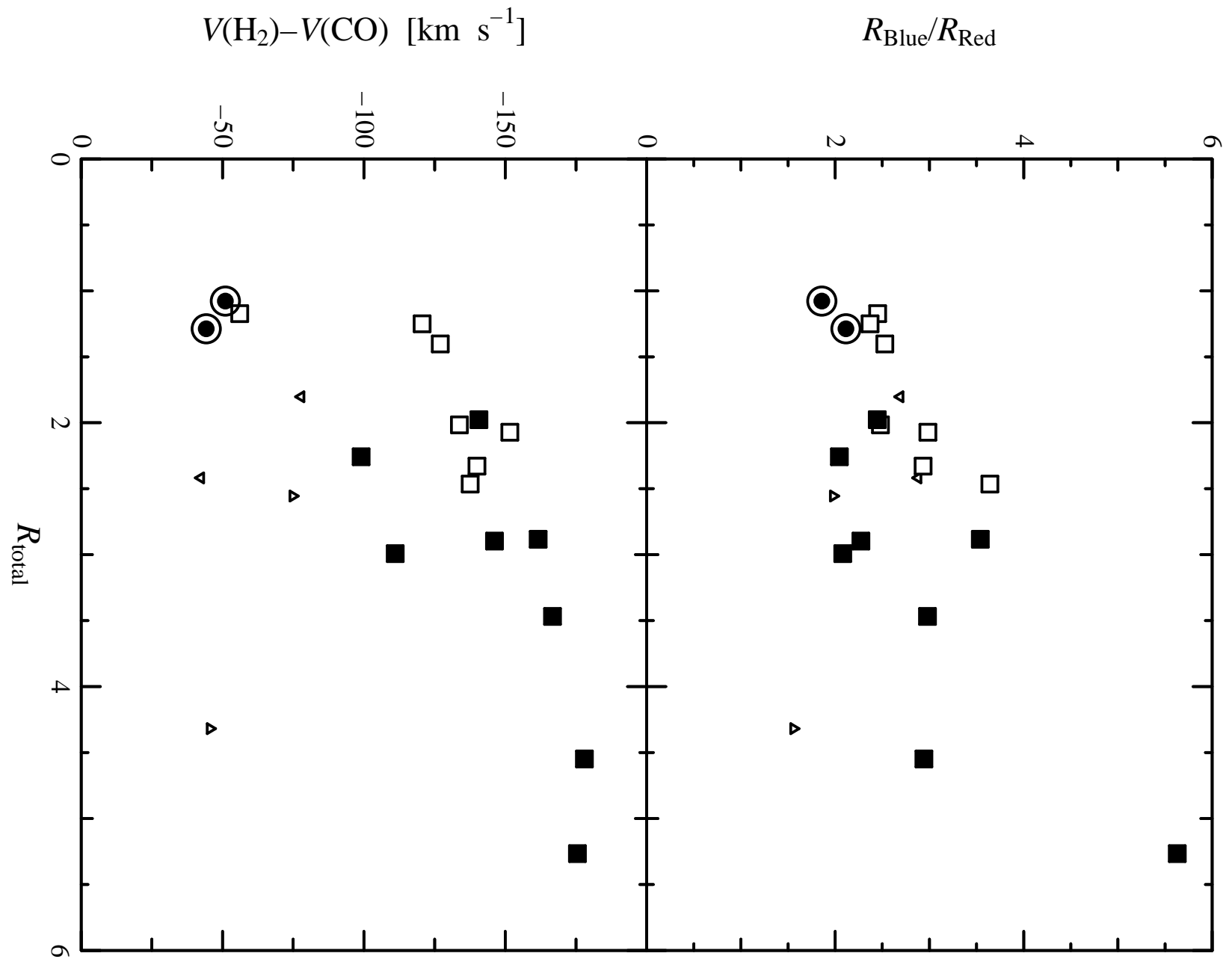




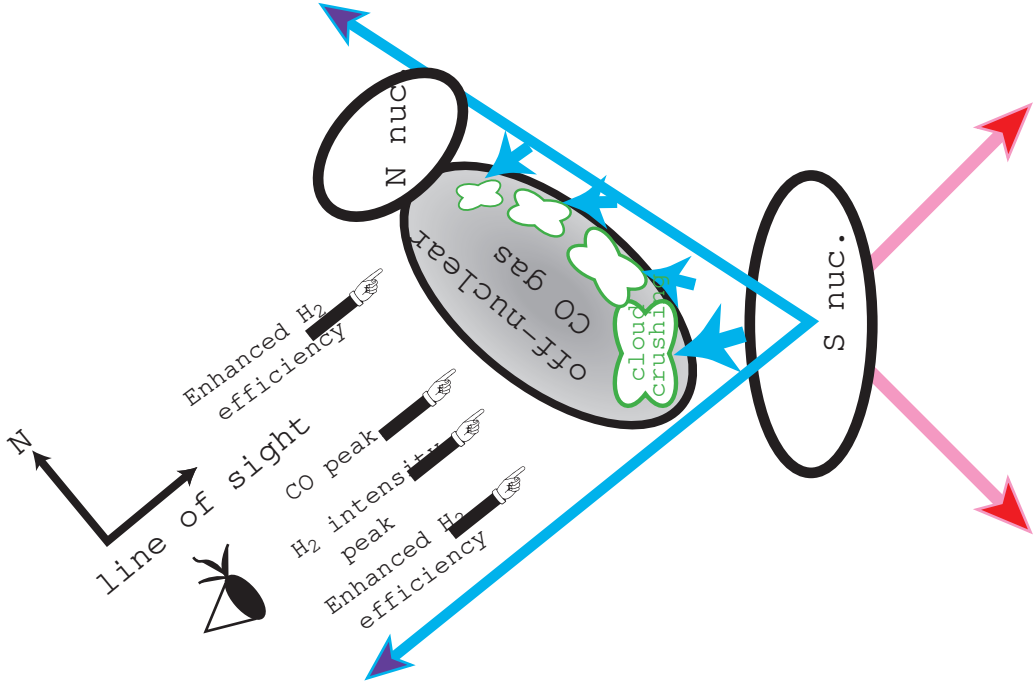








# Side View



Enhanced H<sub>2</sub> efficiency

# Sky View

